AAS 25-202

STUDY OF UNCERTAINTY IN THE PREDICTION OF CISLUNAR TRAJECTORIES USING A LOW-COMPLEXITY ALGORITHM

Brian Baker-McEvilly*, David Canales† and Sirani M. Perera‡

Predicting orbital trajectories presents significant challenges, not only due to computational constraints but also because of uncertainties and perturbations in state measurements. In our previous work, the low-complexity algorithm (LCA) demonstrated its capability to predict trajectories within the three-body problem while significantly minimizing computational complexity. However, it executes exclusively on predefined measurements. This raises questions on the impact of state measurements subjected to perturbations or inaccuracies. In this paper, the potential of the LCA to efficiently determine orbital trajectories while analyzing the impact of such perturbations on state measurements is studied. Thus, the LCA framework is adapted to incorporate uncertainty from perturbations considering interpolated trajectories. This analysis defines a boundary for all trajectories predicted by the LCA under perturbed measurements and characterizes how uncertainties of these state measurements are transformed into trajectories.

INTRODUCTION

In recent history, a renewed focus on the Cislunar region has developed, as seen by the growing list of Lunar missions chartered for the region. Over thirty missions are planned to travel into the region by 2030.[1,2] These missions originated from large-scale, government-funded Lunar programs, such as the United States' Artemis program, Russia's Luna program, and China's Chang'E program. The commercial industry is further contributing to Cislunar traffic through programs such as commercial Lunar payload services (CLPS)[3] and other independent ventures that are sending payloads to the Moon for profit. Companies such as Astrobotics and Intuitive Machines are already adding to the flight heritage of their Lunar landers through missions such as TO2-IM and T02-AB. Furthermore, Cislunar traffic will continue to be perpetuated in the future through the resupplies required at the Artemis Lunar base and other established bases. The growing interest and investment in Cislunar space underscore its importance for scientific, commercial, and military applications.

Modeling the dynamics of Cislunar space requires the consideration of the Earth's and Moon's gravitational influence, and in applications requiring a level of higher fidelity, the Sun's influence. Examples of common Earth-Moon system dynamical models include the circular restricted three-body problem (CR3BP)[1] to represent the gravitational influence of the Earth and Moon upon a

*PhD Student, Aerospace Engineering Department, Embry-Riddle Aeronautical University, Daytona Beach, FL, 32114, USA.

†Assistant Professor, Aerospace Engineering Department, Embry-Riddle Aeronautical University, Daytona Beach, FL, 32114, USA,

‡Associate Professor, Mathematics Department, Embry-Riddle Aeronautical University, Daytona Beach, FL, 32114, USA.

spacecraft, and the bi-circular restricted four-body problem (BCR4BP)[4,5] to represent the gravitational influence of the Earth, Moon, and Sun. These dynamical models are highly nonlinear, sensitive, and do not currently have closed-form solutions. As a result, applications using these models often turn to numerical methods and differential correction tools.[6–11] However, these numerical methods are computationally expensive due to their iterative nature and lack of analytical solutions. The high computational cost of numerical methods may not be viable for the computational bandwidth of every system, or occupy bandwidth that may be utilized by other, more important tasks. To effectively address the challenge of utilizing computationally efficient numerical methods for calculating spacecraft trajectories in the CR3BP, it is essential to realize low-complexity and best-fit algorithms.[12,13]

In astrodynamics, there is a history of using higher-order polynomial interpolation to accurately determine orbital trajectories. Karepova and Kornienko[14] present an introductory analysis of the effect of varying higher-degree polynomials on the accuracy of the Lagrange interpolation method, the traditional method used by global navigation satellite systems. This analysis contains a useful summary of leveraging available state information of a satellite into the interpolation process. Horemuz and Andersson[15] demonstrate using polynomial interpolation between GPS satellite ephemerides, analyzing the accuracy of polynomials of different orders across different time spans. The analysis demonstrated for polynomials of the twelfth order, interpolating over a few hours, a centimeter-level accuracy is achieved between GPS ephemerides. Grzegorz[16] further investigated the use of polynomials in generating trajectories between GPS ephemerides by comparing the accuracy of Bessel, Everett, Stirling, and Newton's interpolation methods. The analysis demonstrated that when predicting across GPS ephemerides separated by 15 minutes, only Stirling, Bessel, and Newton retained millimeter-level accuracy when using a tenth-order polynomial. Grzegorz also demonstrates that the more accurate methods, i.e. Newton and Lagrange, take longer to execute. Despite advancements in these methods, there remains a significant gap in the development of low-complexity spacecraft trajectory generation algorithms.[12,13] This gap is primarily associated with the reliance on computationally intensive polynomial interpolation techniques and the unique boundary conditions derived from state measurements.

It is important to note that the majority of the work on polynomial interpolation is within the near-Earth applications, where trajectories will generally resemble two-body Keplerian trajectories with the consideration of slight perturbations. All of these interpolation algorithms have yet to be tested in a meaningful way on the periodic trajectories presented in the CR3BP that possess unique geometries vastly different than conic sections.[7] Previous work by the authors[12] began to investigate this topic through the developed low-complexity algorithm (LCA) using polynomial interpolation followed by the boundary conditions to accurately determine orbital trajectories in the CR3BP. The LCA demonstrated its ability to replicate CR3BP trajectories to reasonable accuracy when given states separated by many hours of time. Notably, the algorithm reduced computation time by at least 50% compared to traditional numerical integrators for the trajectory generation in all shown cases. Proving to be a potentially viable, computationally efficient, interpolation method within multi-body dynamics when provided with appropriate trajectory data.

This manuscript aims to expand the understanding of the LCA's functionality by investigating the effect of implementing perturbations and uncertainty in the state measurements on the algorithm's stability and capability to produce trajectories. In orbit prediction, state measurements used in the interpolation of a spacecraft's trajectory often contain some form of noise or measurement error that perturbs the anticipated trajectory from its true path.[17,18] Thus, it is paramount to the real-world

application of the LCA to understand how the algorithm handles these uncertainties compared to previous analyses that only considered pre-defined measurements. Implementing perturbations into the LCA further provides insight into stability of the algorithm, demonstrating if small disturbances greatly perturbs the determined trajectory. To lay the foundation of the analysis, the required background on the CR3BP and LCA is provided. Then, the perturbation theory of the LCA is formulated and the setup of the analysis is described. The results of the perturbation analysis are then presented, followed by a discussion of their implications for the stability of the LCA under perturbations. Finally, the work will be completed with a summary of the key results and conclusions.

METHODOLOGY

The Circular Restricted Three-Body Problem

There are many methods of representing motion in the Earth-Moon system, including modeling the influence of the Sun,[19] or coupling attitude and translational dynamics.[20,21] A model that includes the gravitational influence of Earth and Moon is a suitable level of fidelity to represent Cislunar space for the purpose of this work. Thus, the CR3BP is utilized. The CR3BP is comprised of three bodies: a large primary (Earth), a smaller primary (Moon), and a spacecraft of negligible mass. The primaries move about a common barycenter in circular orbits, in which the barycenter is defined using the mass parameter of the system:

$$\mu = \frac{m_M}{m_E + m_M}, \tag{1}$$

where m is the mass and the subscripts E and M refer to the Earth and Moon, respectively. In this manuscript, the equations of motion for the CR3BP are presented in the nondimensionalized Earth-Moon rotating frame. The origin is at the barycenter, with the $+\hat{x}$-axis pointing toward the Moon, the $+\hat{z}$-axis out of the orbital plane, and the $\hat{y}$-axis completing the right-handed system. The system is nondimensionalized using the average Earth-Moon distance for characteristic length, characteristic time ensuring mean motion equals unity, and the combined mass of Earth and Moon for characteristic mass. The nondimensional state of the spacecraft is defined by position $\underline{r} = [x, y, z]^{\mathrm{T}}$ and velocity $\underline{\dot{r}} = [\dot{x}, \dot{y}, \dot{z}]^{\mathrm{T}}$. As a result, the equations of motion are:

$$\ddot{x} = 2\dot{y} + \frac{\partial U^*}{\partial x}, \qquad \ddot{y} = -2\dot{x} + \frac{\partial U^*}{\partial y}, \qquad \ddot{z} = \frac{\partial U^*}{\partial z} \tag{2}$$

in which U^* is the pseudo-potential function of the system given by:

$$U^* = \frac{1-\mu}{||\underline{r}_{E-s/c}||} + \frac{\mu}{||\underline{r}_{M-s/c}||} + \frac{1}{2}(x^2 + y^2) \tag{3}$$

where $\underline{r}_{E-s/c}$ and $\underline{r}_{M-s/c}$ are the position vector from the Earth and Moon to the spacecraft, respectively, and $||\cdot||$ denotes the magnitude of the vector-valued quantities.[1,6] Out of these equations, a constant of integration exists, referred to as the Jacobi constant (JC):

$$JC = 2U^* - (\dot{x} + \dot{y} + \dot{z}). \tag{4}$$

The JC is related to the energy of an object in the CR3BP, and will be used to identify specific trajectories within an orbit family. Finally, five equilibrium solutions exist in the CR3BP, referred to as libration points and denoted $L_1 - L_5$. A schematic of the CR3BP is provided in Figure 1.

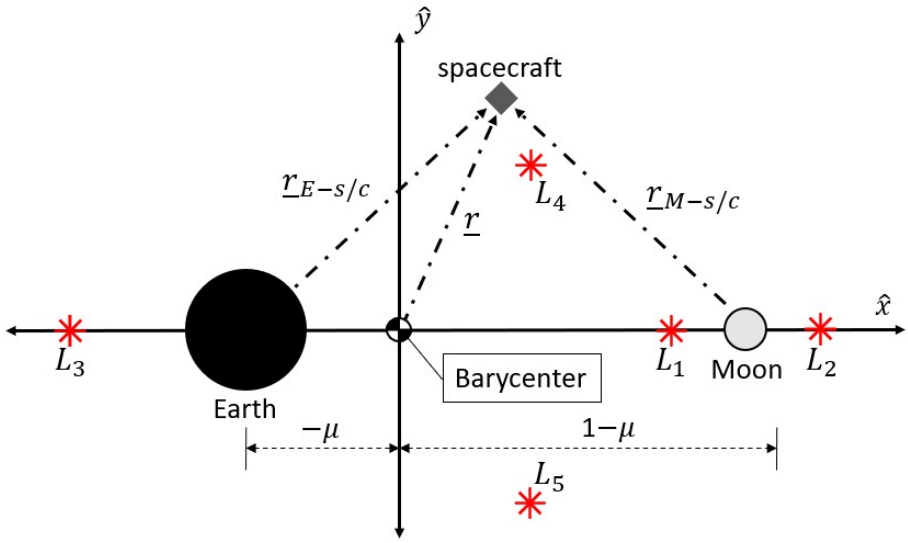

Figure 1: Schematic of the Earth-Moon CR3BP system.

The Low-Complexity Algorithm[12]

The LCA is formulated such that the polynomial satisfies position ($\underline{r}(t_i) = [x(t_i), y(t_i), z(t_i)]^{\mathrm{T}}$), velocity ($\dot{\underline{r}}(t_i) = [\dot{x}(t_i), \dot{y}(t_i), \dot{z}(t_i)]^{\mathrm{T}}$), and acceleration ($\ddot{\underline{r}}(t_i) = [\ddot{x}(t_i), \ddot{y}(t_i), \ddot{z}(t_i)]^{\mathrm{T}}$) of a spacecraft at distinct time t_i, where $i = 0, 1, \cdots, n$, in space of $\mathbb{R}^3$. The trajectory of the spacecraft is defined over n state measurements, described by a set of continuous piecewise functions operating on each interval $I_k = [t_k, t_{k+1}]$, where $k = 0, 1, \cdots, n-1$. The algorithm begins by taking the vectors $\underline{r}(t_i), \dot{\underline{r}}(t_i), \ddot{\underline{r}}(t_i) \in \mathbb{R}^3$ in the non-dimensional form such that $x(t), \dot{x}(t), \ddot{x}(t) \in \mathbb{R}$, and subsequently executes the algorithm in each dimension. Utilizing the fundamental theorem of Lagrange interpolation, a fifth-degree polynomial is presented satisfying the state measurements, i.e., position, velocity, and acceleration based on the boundary at each interval: $I_k = [t_k, t_{k+1}]$. The polynomial in 1D over the interval I_k is defined as:

$$G_k(x(t)) = g_{0,k} + g_{1,k}t + g_{2,k}t^2 + g_{3,k}t^3 + g_{4,k}t^4 + g_{5,k}t^5 \tag{5}$$

and the corresponding velocity and acceleration functions of the spacecraft on interval I_k, respectively, are denoted via

$$\begin{aligned} \dot{G}_k(x(t)) &= g_{1,k} + 2g_{2,k}t + 3g_{3,k}t^2 + 4g_{4,k}t^3 + 5g_{5,k}t^4, \\ \ddot{G}_k(x(t)) &= 2g_{2,k} + 6g_{3,k}t + 12g_{4,k}t^2 + 20g_{5,k}t^3 \end{aligned} \tag{6}$$

where $t_k \leq t \leq t_{k+1}$, and $g_{0,k}, g_{1,k}, \cdots, g_{5,k}$ are the polynomial coefficients that implicitly depend on the position, velocity, and acceleration of the spacecraft on the boundaries of the interval I_k. To determine the coefficients of these polynomials in each interval, and hence to determine the trajectories of the spacecraft over I_k, the known state measurements at t_i are employed as the boundary conditions of each interval at t_k and t_{k+1}. This relationship is summarized as

$$\begin{aligned} G_k(x(t_k)) &= x(t_k) & \qquad G_k(x(t_{k+1})) &= x(t_{k+1}) \\ \dot{G}_k(x(t_k)) &= \dot{x}(t_k) & \qquad \dot{G}_k(x(t_{k+1})) &= \dot{x}(t_{k+1}) \\ \ddot{G}_k(x(t_k)) &= \ddot{x}(t_k) & \qquad \ddot{G}_k(x(t_{k+1})) &= \ddot{x}(t_{k+1}), \end{aligned} \tag{7}$$

where $x(t_k)$, $\dot{x}(t_k)$, and $\ddot{x}(t_k)$ are position, velocity, and acceleration quantities, respectively. Following the system of the equations on interval I_k, an equation using Eq. (5)-(7) is determined s.t.

$$\underbrace{\begin{bmatrix} 1 & t_k & t_k^2 & t_k^3 & t_k^4 & t_k^5 \\ 1 & t_{k+1} & t_{k+1}^2 & t_{k+1}^3 & t_{k+1}^4 & t_{k+1}^5 \\ 0 & 1 & 2t_k & 3t_k^2 & 4t_k^3 & 5t_k^4 \\ 0 & 1 & 2t_{k+1} & 3t_{k+1}^2 & 4t_{k+1}^3 & 5t_{k+1}^4 \\ 0 & 0 & 2 & 6t_k & 12t_k^2 & 20t_k^3 \\ 0 & 0 & 2 & 6t_{k+1} & 12t_{k+1}^2 & 20t_{k+1}^3 \end{bmatrix}}_{A_k} \underbrace{\begin{bmatrix} g_{0,k} \\ g_{1,k} \\ g_{2,k} \\ g_{3,k} \\ g_{4,k} \\ g_{5,k} \end{bmatrix}}_{\underline{g}_k} = \underbrace{\begin{bmatrix} x(t_k) \\ x(t_{k+1}) \\ \dot{x}(t_k) \\ \dot{x}(t_{k+1}) \\ \ddot{x}(t_k) \\ \ddot{x}(t_{k+1}) \end{bmatrix}}_{\underline{b}_k}. \tag{8}$$

where A_k is the coefficient matrix, $\underline{g}_k$ is the vector consisting of the coefficients of the polynomials, i.e., solution of the LCA, and $\underline{b}_k$ is the vector of boundary conditions. By solving Eq. (8), a polynomial that characterizes the trajectories of a spacecraft as it navigates between two boundary conditions, dictated by state measurements, within the interval I_k is found. The LCA executes with a low cost to solve the Eq. (8) while comparing with the brute-force system solving algorithm with $\mathcal{O}(n^3)$ complexity. Further information on the computational efficiency of the LCA, i.e. $\mathcal{O}(n^2)$ complexity, is elaborated upon and demonstrated in our previous work.[12] The LCA achieves its efficiency through the decomposition of the matrix A_k into sparse lower bi-diagonal matrices ($\tilde{L}_k$) and an upper triangular matrix (U_k). This decomposition is given via:

$$U_k \underline{g}_k = \underline{\tilde{b}}_k, \quad \text{where} \quad \underline{\tilde{b}}_k = \left(\prod_{r=1}^{5} \tilde{L}_{r,k} \right) \underline{b}_k \tag{9}$$

where $\underline{\tilde{b}}_k$ is the transformed boundary condition vector. The lower bi-diagonal matrices $\tilde{L}_{r,k} \in \mathbb{R}^{6\times 6}$, $r = 1, 2, .., 5$ and the upper triangular matrix U_k are given in the appendix. The vector of polynomial coefficients is then subsequently solved using the backward substitution through U_k. After the LCA is executed for each dimension in a time interval across all time intervals, a continuous piecewise trajectory of the spacecraft is determined. Pseudo-code for the LCA given an open trajectory (i.e. not a closed loop or no periodic boundary conditions), is in Algorithm 1.

Algorithm 1 LCA pseudo-code for an open trajectory

```
Collect n known state measurements
Break n measurements to k = n − 1 intervals, each containing two boundary conditions that
  are shared with neighboring intervals
for k intervals do
    for Each dimension of the conditions do
        Pre-compute L̃_{r,k} and U_k matrix entries
        Store entries into L̃_{r,k} and U_k matrices
        Compute bidiagonal matrix-vector product, i.e., b̃_k
        Solve for g_k using backward substitution
    end for
end for
```

The conditions required of the system to achieve the shown sparse decomposition are: increments of time that are not approaching zero and chronologically sequenced; and the correct system formulation of two points using position, velocity, and acceleration. The system formulation is required as

the entire decomposition is based on the specifically selected linear system structure, while proper time increments ensure sequential progression of a trajectory in time and avoids singularities in the d_k term. Under these conditions, sparse decomposition is guaranteed.

The LCA is unique from other decomposition techniques in that the structure of the system produces sparse $\tilde{L}$ matrices whose manipulation results in lower arithmetic complexities. The sparse decomposition does not exist for any number of points considered when forming a single polynomial over an interval, or any combination of the state order (i.e. position, velocity, acceleration, jerk, etc.). For example, considering four points for a single interval where position and velocity are known, does not necessarily lead to a system that may be decomposed into sparse matrices. However, there is potential to derive other lower complexity algorithms that factor into sparse diagonal matrices, but this will not always occur.

LOW-COMPLEXITY ALGORITHM PERTURBATION THEORY

Spacecraft state measurements frequently include errors such as noise, perturbations, or other inaccuracies that deviate measurements from the true state. In this scenario, the aim is to analyze the impact of noisy measurements on spacecraft trajectory generation using the LCA. To conduct a quantitative analysis of state measurements, begin by examining the noisy data pertaining to position, velocity, and acceleration, respectively,

$$\begin{aligned} \hat{\underline{r}}(t_i) &= [\hat{x}(t_i), \hat{y}(t_i), \hat{z}(t_i)]^{\mathrm{T}}, \\ \dot{\hat{\underline{r}}}(t_i) &= [\dot{\hat{x}}(t_i), \dot{\hat{y}}(t_i), \dot{\hat{z}}(t_i)]^{\mathrm{T}}, \\ \text{and } \ddot{\hat{\underline{r}}}(t_i) &= [\ddot{\hat{x}}(t_i), \ddot{\hat{y}}(t_i), \ddot{\hat{z}}(t_i)]^{\mathrm{T}} \end{aligned} \tag{10}$$

at distinct times t_i for $i = 0, 1, \cdots, n$. Note that

$$\begin{aligned} \hat{\underline{r}}(t_i) &= \underline{r}(t_i) + \delta\underline{r}(t_i), \\ \dot{\hat{\underline{r}}}(t_i) &= \dot{\underline{r}}(t_i) + \delta\dot{\underline{r}}(t_i), \\ \text{and } \hat{\underline{r}}(t_i) &= \ddot{\underline{r}}(t_i) + \delta\ddot{\underline{r}}(t_i) \end{aligned} \tag{11}$$

are, respectively, the measured state quantities with perturbed position, velocity, and acceleration data given via $\delta\underline{r}(t_i)$, $\delta\dot{\underline{r}}(t_i)$, and $\delta\ddot{\underline{r}}(t_i)$. Given that the LCA relies exclusively on the information from state measurements to determine trajectories, any noise present in these measurements directly impact the generation of the spacecraft trajectory. Thus, the presence of perturbed state measurements, i.e, Eq. (10) with (11), significantly impacts the boundary conditions of the LCA, leading to noisy boundary measurements $\hat{\underline{b}}_k$, expressed as

$$\hat{\underline{b}}_k = \underline{b}_k + \delta\underline{b}_k, \tag{12}$$

for each interval I_k. This results in a distinct polynomial characterized by noisy coefficients $\hat{\underline{g}}_k$, which correspond to the perturbed state measurements $\delta\underline{b}_k$. Thus, variations in the polynomial coefficients cause shifts from the desired path, producing a trajectory that diverges from the original, which can be denoted in $\mathbb{R}$ by

$$\hat{G}_k(\hat{x}(t)) = \hat{g}_{0,k} + \hat{g}_{1,k}t + \hat{g}_{2,k}t^2 + \hat{g}_{3,k}t^3 + \hat{g}_{4,k}t^4 + \hat{g}_{5,k}t^5, \tag{13}$$

where $\hat{G}_k$ represents the interpolated polynomial influenced by variations in state measurements, and $\hat{g}_{0,k}, \hat{g}_{1,k}, \cdots, \hat{g}_{5,k}$ are the new constants determining $\hat{G}_k$. In realistic applications that involve

uncertainty, it is crucial to grasp how variations in the boundary conditions $\hat{\underline{b}}_k$ influence the resulting polynomial $\hat{G}_k$. This understanding is essential for establishing the accuracy of the spacecraft trajectory generation proposed via the LCA.

Using the perturbed boundary conditions derived from the noisy state measurements in Eq.(10) - (12), the matrix equation in Eq. (8) may be perceived as a perturbation of the corresponding linear system given via:

$$A_k\left(\underline{g}_k + \delta\underline{g}_k\right) \quad = \quad \underline{b}_k + \delta\underline{b}_k, \tag{14}$$

where $\delta\underline{g}_k$ is the perturbation of the solution as opposed to the solution obtained via LCA. The matrix equations associated with the LCA (i.e. $A_k\underline{g}_k = \underline{b}_k$ and Eq. (14)) illustrates that the trajectory generation of the spacecraft is subject to perturbations, expressed as $\delta\underline{g}_k = A_k^{-1}\delta\underline{b}_k$. This indicates that any alterations in the boundary conditions lead to proportional adjustments in the coefficients of the polynomial, thereby affecting the solution or the spacecraft's trajectories. In conclusion, by adopting the perturbation theory in [22], the perturbed solution of the system $\delta\underline{g}_k$ in each interval I_k is bounded by

$$\frac{1}{\kappa}\frac{||\delta\underline{b}_k||}{||\underline{b}_k||}||\underline{g}_k|| \leq ||\delta\underline{g}_k|| \leq \kappa\frac{||\delta\underline{b}_k||}{||\underline{b}_k||}||\underline{g}_k||, \tag{15}$$

where $\kappa = ||A_k||\ ||A_k^{-1}||$ is a constant and so-called the condition number of the system in each interval,[23] $\underline{g}_k$ is the solution of the LCA, and $||\cdot||$ denotes the norm. If $e_k := \frac{||\delta\underline{b}_k||}{||\underline{b}_k||}$ is defined as the relative error in the boundary conditions or state measurements, then the relative error in the system is represented by $\frac{||\delta\underline{g}_k||}{||\underline{g}_k||}$. Thus, the deviation of the LCA coefficients from those produced with noise in the state measurements is described as follows:

$$\frac{1}{\kappa}e_k \leq \frac{||\delta\underline{g}_k||}{||\underline{g}_k||} \leq \kappa e_k. \tag{16}$$

Since the LCA interpolation method is calculated based on two boundary conditions for each interval, and these conditions are represented as vector-valued quantities, the perturbation of these quantities also become vector-valued, provided the norm as indicated in Eq. (15) is disregarded. Thus, the impact of vector-valued quantities are to be investigated, particularly focusing on how the direction of vector-valued perturbation quantities in each boundary condition affects the resulting polynomial. For example, consider a perturbation in position in the $\hat{x}$-direction of 5 m applied to the initial and final boundaries. If these perturbations shift the boundary conditions toward each other, the resulting polynomial will differ from the one obtained if the boundary conditions are pushed apart. The numerical analysis of arbitrary state measurement perturbations at both initial and final boundaries reveals that the most severe perturbation occurs when the position and acceleration changes align in the same direction, while the velocity changes operate in opposing directions.

PERTURBATIONS IN THE BOUNDARY CONDITIONS ANALYSIS

In real-world applications, the state measurements provided to the LCA contain noise or uncertainty that alters the states from their true values. These perturbed measurements implemented into the LCA perturb the coefficients of the polynomial, and thus the trajectory generated by the LCA. Therefore, this analysis distinctly investigates the variations in polynomial coefficients as well as the variations in the spatial trajectories as a result of perturbed measurements. The LCA's response

to a set of perturbations also implies its numerical stability, in which a numerically stable LCA with a disturbance in the boundary conditions will lead to a proportionally small change in polynomial coefficients. With these goals in mind, perturbations are applied to the boundary conditions of the LCA. In this analysis, trajectories from previous work[12,13] are utilized as their functionality with the LCA is well-reviewed and understood. This includes a distant retrograde orbit (DRO) with a Jacobi Constant of 2.9337, an L_4 axial orbit with a Jacobi constant of 2.0941, and an L_2 southern near-rectilinear halo orbit (NRHO) with a Jacobi constant of 3.0455. Additionally, from previous analysis, it is generally understood that the accuracy of the LCA diminishes in dynamically sensitive regions, or when the jerk of a trajectory is large.

Variations in Coefficients

Equation (16) establishes limits on the perturbation of boundary conditions in relation to the predefined conditions, depending on whether the orbital trajectory generation system is well-conditioned or ill-conditioned. Assume the system is well-conditioned and satisfies Equation (16), how the perturbations in the boundary conditions influence the solution of the system may be analyzed. Therefore, this investigation aims to validate the boundary conditions in Eq. (16), and gain an understanding of the resulting perturbation to the polynomial coefficients and orbital trajectory caused by the variation in the state measurements. To achieve this goal, an arc along the L_4 Axial orbit and the NRHO are considered (Figure 2). The L_4 Axial arc is selected since it is a section that the LCA interpolates efficiently, while the NRHO arc is selected as it poses more of a challenge for the LCA. It is known that the resulting coefficient perturbations ($\delta \underline{g}$) pose a dependency on which entries in the boundary conditions ($\underline{b}$) are perturbed. That is, a perturbation in initial and final position yields a different perturbation in coefficients than a perturbation in initial and final velocity. To accom-

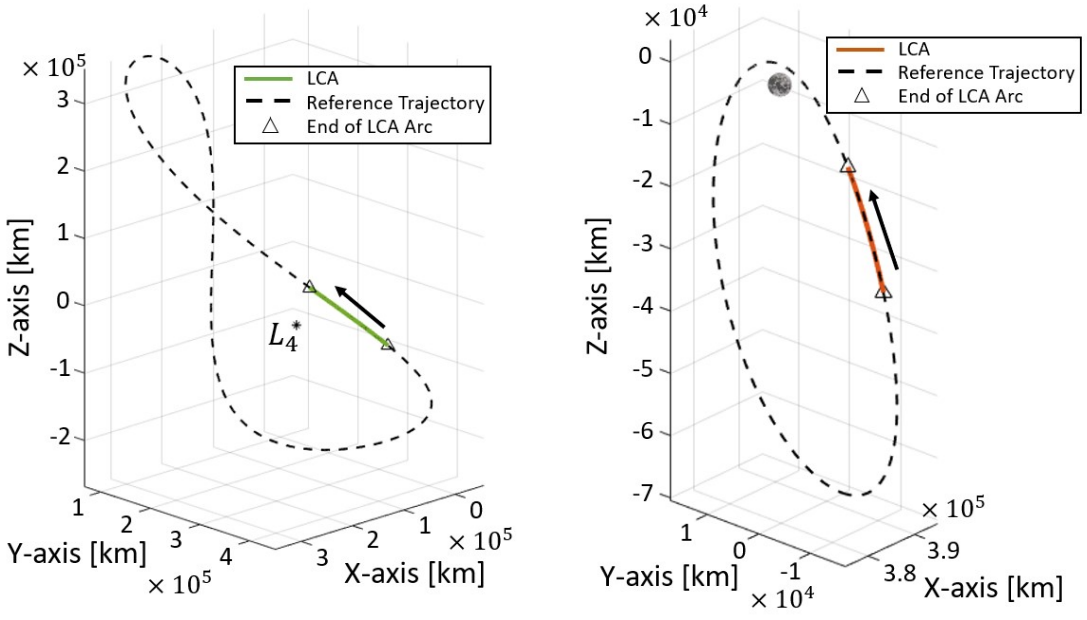

(a) L_4 Axial reference and LCA trajectory.

(b) NRHO reference and LCA trajectory.

Figure 2: The selected sections of the L_4 Axial and NRHO sampled for analysis on the impact of perturbations on the LCA coefficients.

modate this effect in the analysis, three different perturbations profiles are analyzed. These profiles are comprised of scenarios perturbing only either position, velocity, or acceleration. For simplicity, the perturbation magnitude is also evenly distributed between the initial and final conditions. Using these different boundary condition perturbations ($\delta\underline{b}$), the relative error of the coefficients described in Eq. (16) is determined and shown in Figure 3 for the two selected arcs. For these cases, it is seen that there are slight variations in this analysis across the three dimensions of the trajectory. Thus, for the sake of brevity, only the analysis in the z-direction is shown. The z-direction is selected as both trajectories possess significant motion in the z-component.

The results validate the boundary defined by Eq. (16), demonstrating that for these two arcs, the system is well-conditioned. This implies that a small perturbation in the measurements results in a proportional perturbative response. When observing each perturbation case across the selected arcs, perturbations in velocity result in the largest relative coefficient error, followed by acceleration, and finally position perturbation. This indicates that the velocity possesses the most significant influence over the coefficients than any other parameter. Additionally, the LCA reaches instability faster due to increasing variations in velocity. Regardless, each case is sufficiently encompassed by the bounds determined in Eq. (16). When comparing the two arcs, it is generally seen that, given a perturbation, the NRHO arc yields a higher relative coefficient error than the Axial arc. This pattern further solidifies the conclusion drawn in previous work[12] that the LCA struggles to handle trajectories that are rapidly changing or dynamically sensitive. As in this case, the dynamically milder L_4 Axial arc yields a smaller relative coefficient error compared to the dynamically more sensitive NRHO arc.

The conditioning of the system for the LCA is dependent upon the initial and final time of the LCA arcs, as they are what form A_k in Eq. (8). The analysis presented in Figure 3 examines an arc over a specific time, which could inherently result in a well-conditioned system. To ensure that shifts in the arc's duration do not result in a serious shift from the results shown in Figure 3, further analysis is required. Consider the same arcs in Figure 2, except now the initial boundary condition of the arc remains unchanged, while a new final boundary condition is established based

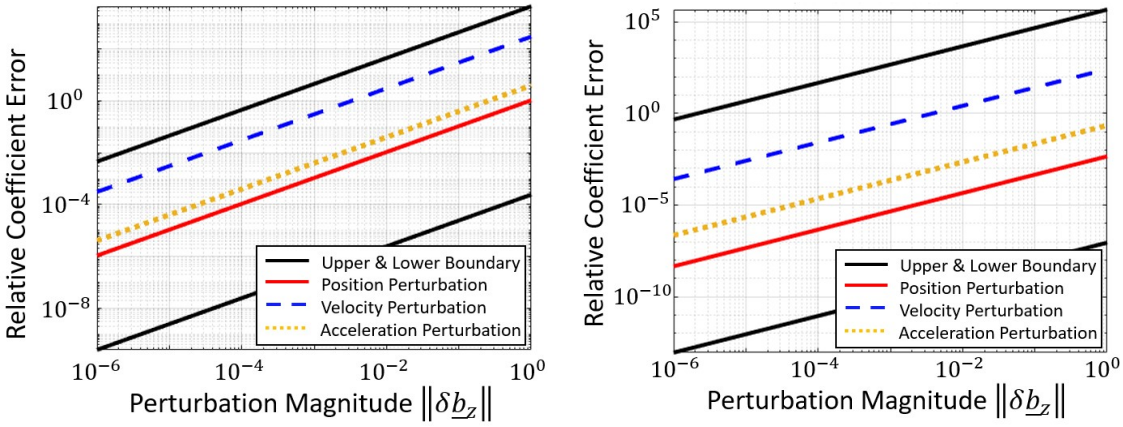

(a) L_4 Axial relative error in z-coefficients due to perturbations, where $||\underline{b}_z|| = 0.944$.

(b) NRHO relative error in z-coefficients due to perturbations, where $||\underline{b}_z|| = 4.85$.

Figure 3: The relative coefficient error for the selected arcs due to variations in the perturbation magnitudes and perturbation types.

on a specified period for the arc. Analyzing only the z-direction across this new arc, a perturbation magnitude ($||\delta \underline{b}_z||$) of 10^{-4} is selected, as 10^{-4} is a reasonably small perturbation and produced well-behaved results in Figure 3. The resulting coefficient boundary and relative coefficient error due to different arc time spans are shown in Figure 4. It is seen that the boundaries of the coefficients become tighter as the time span increases.

The cause of the tighter boundary is either the result of the boundary condition norm ($||\underline{b}_z||$) becoming larger and causing the perturbation ($||\delta \underline{b}_z||$) to have less of an impact, or the conditional number of the system becomes larger. Both possibilities must affect the size of the boundary, but the conditional number growing is the dominant effect since as the time span shrinks, the LCA approaches the singularity in the d_k, and the system will become ill-conditioned. Furthermore, the behavior persists across the simulated orbits, and the boundary condition norm does not always increase when the duration of the arc is shrunk. To demonstrate this, the boundary condition norm for the L_4 axial and NRHO for each arc duration is shown in Figure 5. In Figure 5a, even while the relative boundary condition error of the axial orbit is growing and shrinking, the relative coefficient error boundary in Figure 4a is becoming larger as the time span shrinks. However, the plots demonstrate that no unprecedented behavior occurs when changing the time span of the arc, but caution over the conditioning of the system must be used when shrinking an arc's time span significantly. Variations in the coefficient boundary and relative error occur, but not in a manner to warrant concern over different time spans of an LCA arc.

In conjunction, this perturbation analysis investigating the error in coefficients, along with the accuracy analysis shown in previous work,[12] demonstrates the numerical stability of the LCA. The perturbation analysis worked to prove that given a reasonable time span of an arc, the LCA is a well-conditioned system in which a small perturbation yields a small variation in response. Furthermore, the accuracy analysis in previous work[12] demonstrates that the LCA may accurately reproduce an arc of interest, relative to the overall span of the arc. Naturally, there are limitations to this stability. Trajectories that are not sampled appropriately during rapidly changing sections will produce unreasonable errors, as seen along the perilune example of the NRHO. Additionally, introductions

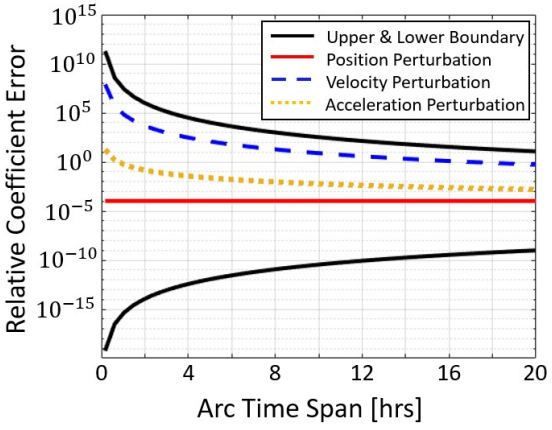

(a) L_4 Axial relative error in z-coefficients with variation in time span.

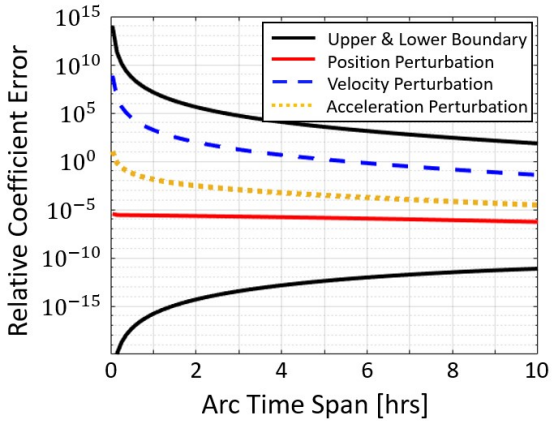

(b) NRHO relative error in z-coefficients with variation in time span.

Figure 4: The relative coefficient error for the selected arcs due to variations in the time span of the generated arc, where $||\delta \underline{b}_z|| = 10^{-4}$.

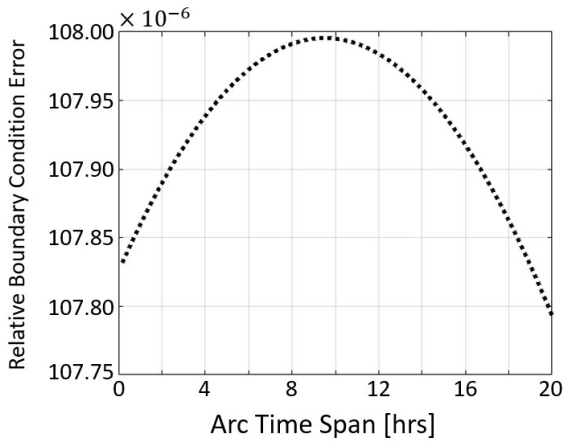

(a) L_4 Axial relative error in z-boundary conditions with variation in time span.

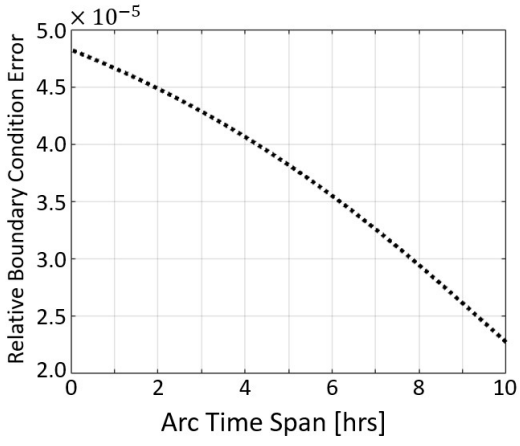

(b) NRHO relative error in z-boundary condition with variation in time span.

Figure 5: The relative boundary condition error ($e_k = {||\delta \underline{b}_z||}/{||\underline{b}_z||}$) for the selected arcs due to variations in the time span of the generated arc, where $||\delta \underline{b}_z|| = 10^{-4}$.

of perturbations that are much larger than the norm of the boundary condition yield significantly perturbed coefficients. However, for a well-posed interpolation problem, the LCA behaves in a numerically stable manner.

Variations in Spatial Trajectories

Previously, the perturbation analysis only considers the variation in the norm of the polynomial coefficients due to the introduction of perturbations in the state measurements. This provides context on the general impact of perturbations on the algorithm's ability to determine the polynomial coefficients, but no insight into how a change in coefficients then transform into a physically perturbed trajectory is demonstrated. Each coefficient holds an influence over the trajectory and perturbations uniquely effect these coefficients in different manners. Therefore, the following analysis aims to relate a perturbation in state measurements to a physical perturbation in the LCA generated trajectory. Specifically, the analysis will define a boundary in which under a perturbation, all potential trajectories abiding by the perturbation shall remain within. To achieve this, consider a small piece of a DRO that spans slightly over 21 $hours$, shown in Figure 6. This arc acts as a simple planar case such that the conclusions drawn from this arc may expand to more complex trajectories.

Perturbations for the selected initial and final boundary conditions are now determined. Position and velocity perturbations are chosen based on magnitudes that are appropriate for the respective parameters and that yield informative results. The acceleration perturbation is determined using the CR3BP equations of motion, implementing the true and perturbed position and velocity quantities at the initial and final time. These conditions are plugged into the CR3BP and a resulting change in acceleration is calculated. The perturbations are expressed as an ellipse about the true quantity. For simplicity, the minor and major axis are determined by the perturbation magnitude along the x-axis and y-axis. The chosen perturbation magnitudes in this analysis are shown in Table 1. It is important to note that the effect of the perturbations on the arc generated by the LCA is determined by the perturbation magnitudes, direction, and the interaction of different magnitude and direction

Table 1: Perturbation magnitudes for initial and final points.

Point	$\delta x\ [m]$	$\delta v_x\ [\frac{m}{s}]$	$\delta y\ [m]$	$\delta v_y\ [\frac{m}{s}]$
Initial	500	80	800	60
Final	800	60	500	80

selections at the initial and final measurement.

To obtain an initial understanding of the effect perturbations have on the LCA, the initial and final measurements of the DRO arc are perturbed according to the values shown in Table 1. For both initial and final points, the state measurements are perturbed in a random direction, by a random magnitude. The direction determines the maximum allowed magnitude, outlined by the perturbation ellipse previously stated. The LCA then determines the the trajectory using the perturbed state measurements. This process is repeated numerous times, producing many perturbed trajectories. From the previous work,[12] it is generally seen that an LCA trajectory deviates the most from the reference at the mid-point of the arc's time span. Therefore, to analyze a snapshot of all the perturbed trajectories at the likely worst-case scenario, the states of the perturbed trajectories are determined at the mid-point of the selected arc's timespan ($\approx 10\ hours$). These states are subsequently shown in Figure 7, shifted such that the position of the unperturbed LCA at this instance in time is at the origin. Since the LCA decouples the coordinate systems and interpolates the polynomial in a single dimension at a time, the perturbations applied to the state measurements are also be decoupled. This means that a perturbation in a given dimension directly determines the perturbation from the reference trajectory in that same dimension. Hence, in Figure 7, a shift in the x-axis and y-axis from the origin directly correlates to (δx, δv_x, δa_x) and (δy, δv_y, δa_y), respectively. It is clear from the distribution of points that some boundary exists in the simulation that encompasses all of the perturbed trajectories. However, the perturbed trajectories will not simply be defined by the worst case perturbation to position, velocity, or acceleration as the interaction between the perturbations at the initial and final point also play a role. Thus, to determine the explicit boundary of the perturbed trajectories using the LCA, the effect of each perturbation on the trajectory is investigated.

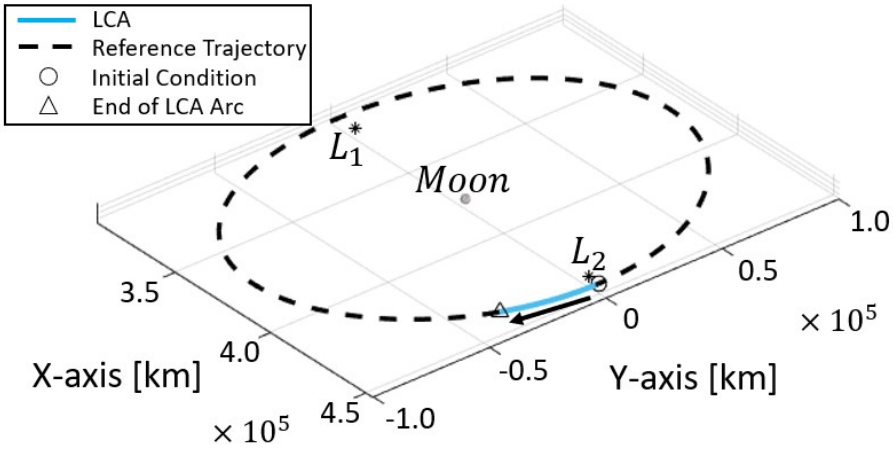

Figure 6: Reference trajectory of a DRO and the section of DRO that is later perturbed.

The relationship between initial and final perturbations, as well as their magnitude, are analyzed by determining the resulting change in a trajectory due to variations in each parameter. Since the dimensions are decoupled within the LCA, the analysis is further broken down into the interactions of the initial and final x-perturbations and y-perturbations. The same analysis is conducted once more, perturbing the arc's initial and final states, based upon magnitudes discussed in Table 1. The perturbations are shifted across a single variable at a time, that is only perturbing either position, velocity, and acceleration in each simulation. Furthermore, the perturbations between initial and final measurements are varied. The position of the perturbed trajectory is recorded at the mid-point of the time interval, and the error is determined from the unperturbed trajectory. The results of this analysis are summarized in Figure 8 where x-perturbations are shown with a yellow-green gradient and y-perturbations are shown with a cyan-purple gradient.

An explicit boundary for the analyzed set of perturbations is present within Figure 8. In terms of perturbation magnitude, the boundary is formed using the largest available perturbation, as such magnitude correspond to the largest error. In terms of perturbation direction, the boundary requires a different combination of perturbation directions within position, velocity, and acceleration. For position, the maximum error occurs when the initial and final perturbations are perturbed in the same direction, either positively or negatively. Although the evolution of the error varies, this maximum error occurring at similarly signed position perturbations is consistent across x-perturbation and y-perturbation cases. Looking to the velocity, it is apparent that the maximum error occur when the initial and final velocity are perturbed in opposite directions. Once again, the complete map of error magnitude varies between x-perturbations and y-perturbations, but the maximum error occurring at opposite velocity directions is consistent. Finally, the acceleration is similar to the position in that the maximum error occurs when the initial and final acceleration perturbations are in the same direction. It shall also be noted that there is a straight cut through the data shown in Figure 8, where there is no perturbation from the unperturbed LCA, even under perturbed initial and final quantities. This is because these plots are only snapshots of the middle of the time interval. So

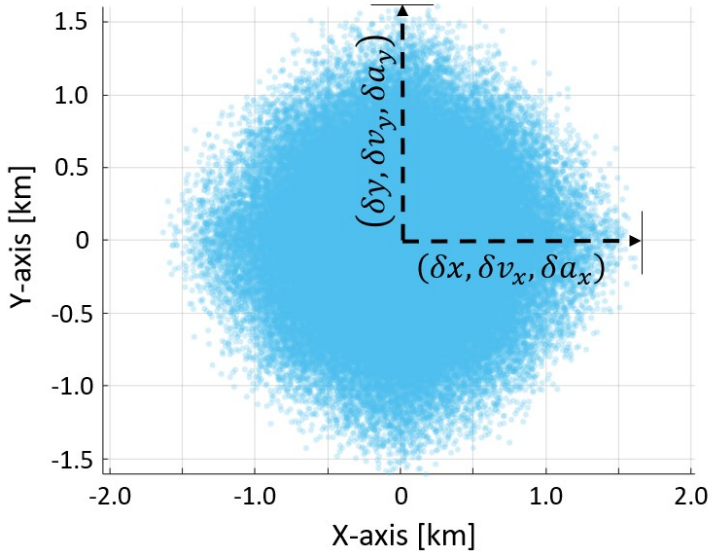

Figure 7: Position of the perturbed trajectories at the middle of the time interval ($\approx 10\ hours$), where the unperturbed trajectory is at the origin.

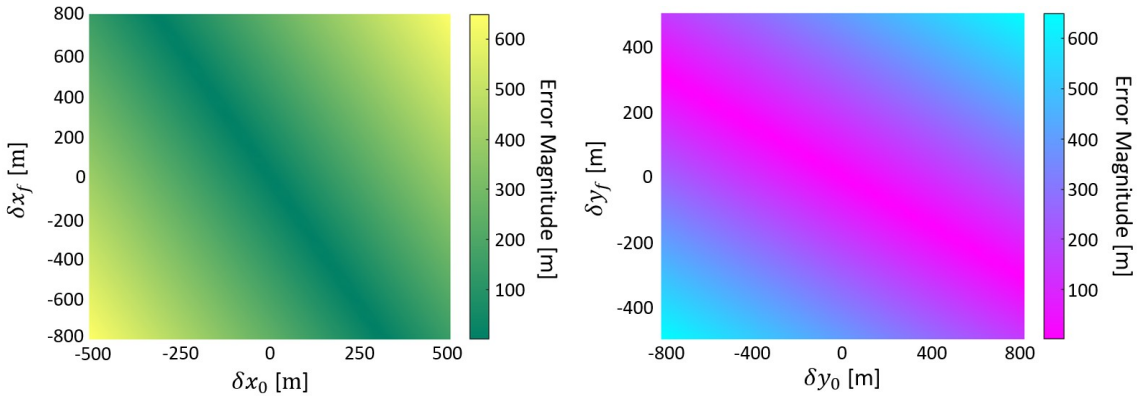

(a) Variation in x position.

(b) Variation in y position.

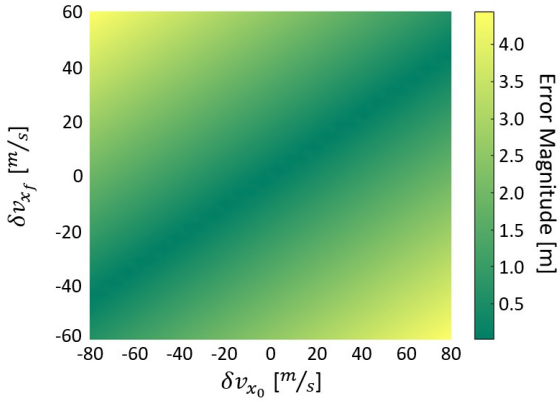

(c) Variation in x velocity.

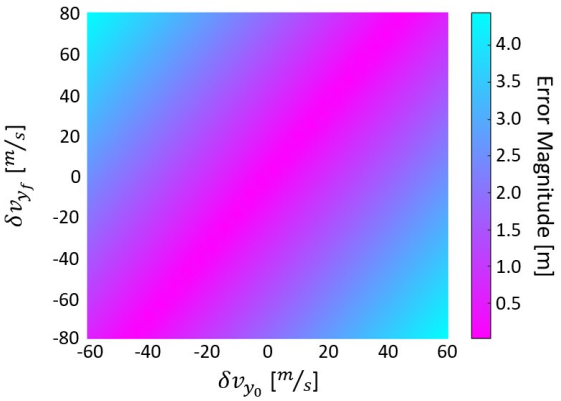

(d) Variation in y velocity.

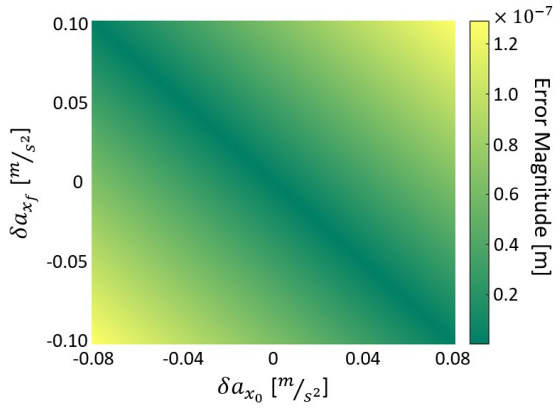

(e) Variation in x acceleration.

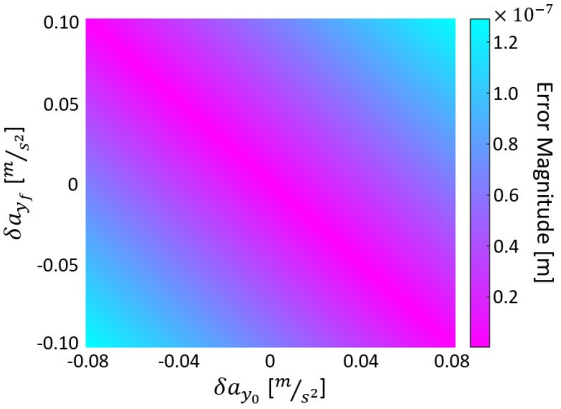

(f) Variation in y acceleration.

Figure 8: Deviation from reference LCA trajectory due to varying the perturbations applied to initial and final measurements, analyzed at the mid-point of the time interval.

there are combinations of perturbations that produce the same position as the unperturbed arc at this instance in time, but the arcs evolve differently throughout the sections of trajectory not shown.

The combination of perturbations that lead to the maximum error describes the boundary that contains any potential trajectories produced from combinations of perturbations. Therefore, in this simulation, the boundary is described by an LCA trajectory that is generated using the largest perturbations, in which the initial and final perturbations have opposite velocity directions and similar position and acceleration directions. In other words, the boundary is defined by the LCA arcs generated using the set of perturbations given by:

$$\begin{aligned} x_{Boundary} &= \pm[\delta x_{0-max},\, \delta x_{f-max},\, \delta v_{x_{0-max}},\, -\delta v_{x_{f-max}},\, \delta a_{x_{0-max}},\, \delta a_{x_{f-max}}], \\ y_{Boundary} &= \pm[\delta y_{0-max},\, \delta y_{f-max},\, \delta v_{y_{0-max}},\, -\delta v_{y_{f-max}},\, \delta a_{y_{0-max}},\, \delta a_{y_{f-max}}]. \end{aligned} \quad (17)$$

To demonstrate the boundary determined by Eq. (17), consider the results shown in Figure 7. In this work, the perturbations are described as an ellipse around the initial and final state respectively. The evolution of this boundary, according to Eq. (17), encompasses all potential trajectories that adhere to these perturbations.

The LCA decouples the evolution of each dimension, ensuring that as these elliptical boundaries progress along the trajectory, rotation is not possible. This implies that a point at a certain angle about the initial perturbation ellipse shall map to the same point at the same angle in the final perturbation ellipse. Furthermore, each set of mapped points along the ellipse boundary possesses a unique maximum perturbation for position, velocity, and acceleration. Thus, the boundary comprised of mapped points evolves in its totality according to each respective arc generated by the LCA when the perturbations of each set of mapped points follow Eq. (17). To demonstrate this, consider a boundary that evolves in this manner, and its form in the middle of the time interval for the selected DRO arc. The boundary is formed according to each LCA arc generated between respective mapped points, and is shown in Figure 9. As anticipated, the boundary encompasses all of the perturbed trajectories. Through closer analysis of this simulation, this explicit boundary is demonstrated to be true for the entire duration of the arc. Figure 10 exhibits the evolution of the boundary, sample perturbed trajectories, and unperturbed trajectories for the entire time span of the arc. Overall, this method to determine a boundary of trajectories generated by the LCA given a set of perturbations is valid for other arcs and trajectories. The process for then extending this result into three-dimensional trajectories is simple as, once again, the LCA handles every dimension independently. Therefore, the boundary perturbations in Eq. (17) is extended to include the new dimension and the LCA trajectories that describe the boundary will now be ran for the additional dimension.

One of the weaknesses of the LCA is that it does not directly take into the consideration the dynamical model governing the motion of the trajectory. The algorithm takes only measurements, decouples the dimensions, and interpolates accordingly at a lower cost. Thus, the LCA is unable to properly incorporate statistical distributions of measurements, sometimes expressed as perturbation, that are non-deterministic and are physically coupled through the dynamics. Throughout the analysis shown in this work, the perturbations are deterministic, bounded, and decoupled. Consequently, the results and conclusions may not be directly applicable to trajectories derived from measurements that exhibit statistical variability, such as those from onboard GNC systems. Despite the limitation in application to realistic measurements, the analysis demonstrates that under perturbations, the LCA is a stable and well-conditioned algorithm. A conclusion that is still vital to the understanding of the LCA's functionality and a key take-away of this work.

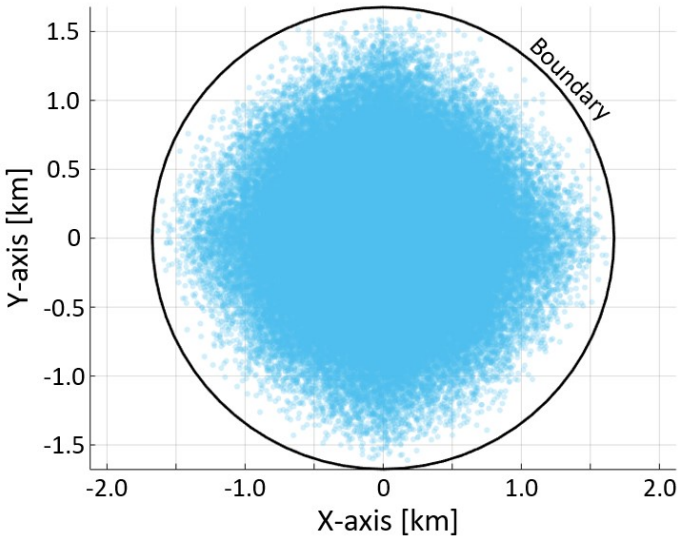

Figure 9: Position of the perturbed trajectories and explicit perturbation boundary at the middle of the time interval ($\approx 10\ hours$), where the unperturbed trajectory is at the origin.

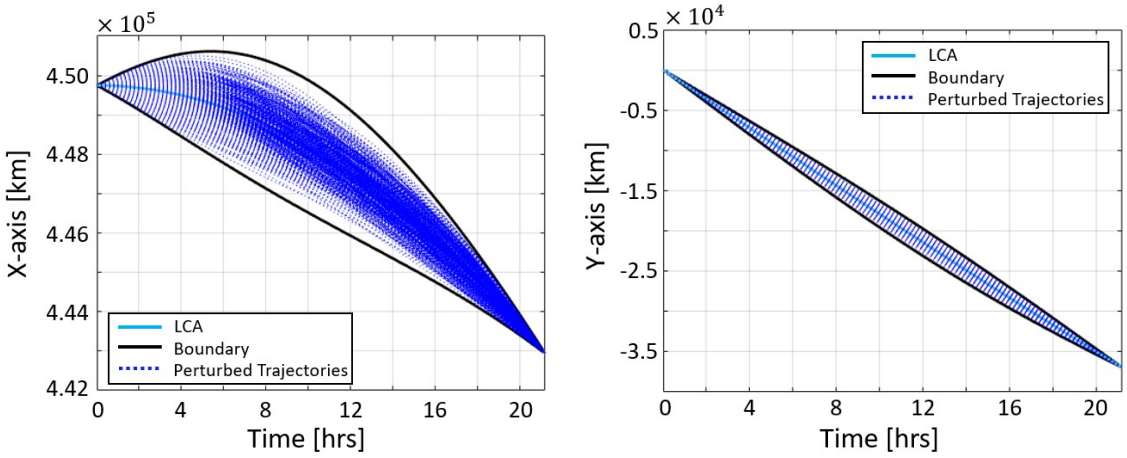

(a) Trajectories along x-axis with time.

(b) Trajectories along y-axis with time.

Figure 10: Demonstration of boundary satisfaction for perturbed trajectories throughout the analyzed arc within a DRO, presented in the Earth-Moon rotating frame.

CONCLUSION

In most applications, spacecraft state measurements are subject to uncertainties that deviate them from the true or mean state. Since the LCA predicts a trajectory using only information on state measurements, changes in these measurements directly impact the LCA's trajectory generation capabilities. Therefore, understanding the effect of perturbations and uncertainties in the LCA is paramount to understanding its application and stability. Two investigations are conducted: first, looking into the effect of perturbations on the polynomial coefficients generated by the LCA; and second, exploring how the perturbed coefficients impact the spatial trajectories themselves. Ob-

serving the effect of perturbation on the coefficients shows the algorithm is well-conditioned, as the relative coefficient error remained within the described bounds and a change in boundary conditions yielded some proportional change in coefficient error. Thus, a small perturbation in boundary conditions leads to a small change in coefficients. The velocity is also demonstrated to have the heaviest weight in the perturbation of the polynomial coefficients. The investigation into the perturbation of physical trajectories determined that for a set of known perturbations, a boundary may be formed that encompasses all potential trajectories. Each piece of this boundary then evolves from the initial to the final boundary condition according to the LCA arc generated using the perturbations listed in Eq. 17.

The perturbation results suggest that the LCA is a well-conditioned algorithm where a small perturbation results in a minor change in the solution vector, or the polynomial coefficients that describe a trajectory. In conjunction with the sufficient accuracy results in previous work,[12] it may be said that the LCA is a stable algorithm. Furthermore, it is important to note that the perturbation conclusions may only extend to the subject of stability for the LCA, and not to the physical evolution of the perturbations. This is primarily because the uncertainty of real measurements, represented as perturbations, is statistical and interconnected through the dynamics of the system. The LCA is not able to express this transformation of statistical variation from initial to final boundary conditions as it decouples the dimensions without regard to the dynamical model.

ACKNOWLEDGMENT

This work was partially funded by the National Science Foundation Science with the award number 2410676.

APPENDIX

In order to complete the matrix vector product $(\prod_{r=1}^{5} \tilde{L}_{r,k})\underline{b}_k = \tilde{L}_5 \cdots \tilde{L}_1 \underline{b}_k$ and backwards substitution through the system $U_k \underline{g}_k = \tilde{\underline{b}}_k$, the pre-computed matrix entries of $\tilde{L}_{r,k}$ and U_k must be defined. The matrices $\tilde{L}_{r,k} \in \mathbb{R}^{6\times 6}$, $r = 1, 2, .., 5$ and U_k are given via

$$\tilde{L}_{1,k} = \begin{bmatrix} 1 & & & & & \\ -d_k & d_k & & & & \\ & & 1 & & & \\ & & -d_k & d_k & & \\ & & & & 1 & \\ & & & & -d_k & d_k \end{bmatrix}, \quad \tilde{L}_{2,k} = \begin{bmatrix} 1 & & & & & \\ & 1 & & & & \\ & d_k & -d_k & & & \\ & & & 1 & & \\ & & & d_k & -d_k & \\ & & & & & 1 \end{bmatrix},$$

$$\tilde{L}_{3,k} = \begin{bmatrix} 1 & & & & & \\ & 1 & & & & \\ & & 1 & & & \\ & & -2d_k & d_k & & \\ & & & & 1 & \\ & & & & -2d_k & d_k \end{bmatrix}, \quad \tilde{L}_{4,k} = \begin{bmatrix} 1 & & & & & \\ & 1 & & & & \\ & & 1 & & & \\ & & & 1 & & \\ & & & 3d_k & -d_k & \\ & & & & & 1 \end{bmatrix},$$

$$\tilde{L}_{5,k} = \begin{bmatrix} 1 & & & & & \\ & 1 & & & & \\ & & 1 & & & \\ & & & 1 & & \\ & & & & 1 & \\ & & & & -2d_k & d_k \end{bmatrix}, \quad U_k = \begin{bmatrix} 1 & t_0 & t_0^2 & t_0^3 & t_0^4 & t_0^5 \\ & 1 & c_{1,k} & c_{2,k} & c_{3,k} & c_{4,k} \\ & & 1 & e_{1,k} & e_{2,k} & e_{3,k} \\ & & & 1 & 2c_{1,k} & f_k \\ & & & & 2 & 2m_k \\ & & & & & 2 \end{bmatrix} \tag{18}$$

where the pre-computed entries are given by

$$\begin{aligned} d_k &= \frac{1}{t_{k+1} - t_k}, \\ c_{1,k} &= t_{k+1} + t_k, \\ c_{2,k} &= t_{k+1}^2 + t_{k+1}t_k + t_k^2, \\ c_{3,k} &= t_{k+1}^3 + t_{k+1}^2 t_k + t_{k+1}t_k^2 + t_k^3, \\ c_{4,k} &= t_{k+1}^4 + t_{k+1}^3 t_k + t_{k+1}^2 t_k^2 + t_{k+1}t_k^3 + t_k^4, \\ e_{1,k} &= t_{k+1} + 2t_k, \\ e_{2,k} &= t_{k+1}^2 + 2t_{k+1}t_k + 3t_k^2, \\ e_{3,k} &= t_{k+1}^3 + 2t_{k+1}^2 t_k + 3t_{k+1}t_k^2 + 4t_k^3, \\ f_k &= 3t_{k+1}^2 + 4t_{k+1}t_k + 3t_k^2, \\ m_k &= 2t_{k+1} + 3t_k. \end{aligned} \tag{19}$$

REFERENCES

[1] B. Baker-McEvilly, S. Bhadauria, D. Canales, and C. Frueh, "A comprehensive review on Cislunar expansion and space domain awareness," *Progress in Aerospace Sciences*, Vol. 147, 2024, https://doi.org/10.1016/j.paerosci.2024.101019.

[2] B. Baker-McEvilly, S. Doroba, A. Gilliam, F. Criscola, D. Canales, C. Frueh, and T. Henderson, "A review on hot-spot areas within the Cislunar region and upon the Moon surface, and methods to gather passive information from these regions," *AAS/AIAA 33rd Space Flight Mechanics Meeting*, 2023.

[3] NASA, "Audit of NASA's CLPS Initative," *United States Office of The Inspector General, Office of Audits*, Vol. IG-24-013, 2024.

[4] K. K. Boudad, *Trajectory Design Between Cislunar Space and Sun-Earth Libration Points in the Four-Body Model*. PhD thesis, Purdue University, 2022.

[5] K. Boudad, K. C. Howell, and D. C. Davis, "Analogs for Earth-Moon Halo Orbits and their Evolving Characteristics in Higher-Fidelity Force Models," *AIAA SCITECH 2022 Forum*, 2022, 10.2514/6.2022-1276.

[6] D. Canales, *Transfer Design Methodology Between Neighborhoods of Planetary Moons in the Circular Restricted Three-Body Problem*. PhD thesis, Purdue University, 2021.

[7] D. Grebow, "Generating Periodic Orbits in the Circular Restricted Three-Body Proglem with Application to Lunar South Pole Coverage," Master's thesis, Purdue University, 2006.

[8] B. G. Marchand, K. C. Howell, and R. S. Wilson, "Improved Corrections Process for Constrained Trajectory Design in the n-Body Problem," *Journal of Spacecraft and Rockets*, Vol. 44, No. 4, 2007, pp. 884–897, 10.2514/1.27205.

[9] J. M. Aristoff, J. T. Horwood, and A. B. Poore, "Orbit and uncertainty propagation: a comparison of Gauss-Legendre-, Dormand-Prince-, and Chebyshev-Picard-based approaches," *Celestial Mechanics and Dynamical Astronomy*, Vol. 118, Jan. 2014, pp. 13–28, 10.1007/s10569-013-9522-7.

[10] B. Macomber, R. M. Woollands, A. Probe, A. Younes, X. Bai, and J. Junkins, "Modified Chebyshev Picard Iteration for Efficient Numerical Integration of Ordinary Differential Equations," *Advanced Maui Optical and Space Surveillance Technologies Conference*, Sept. 2013.

[11] A. Atallah, R. Woollands, T. Elgohary, and J. Junkins, "Accuracy and Efficiency Comparison of Six Numerical Integrators for Propagating Perturbed Orbits," *Journal of the Astronautical Sciences*, Vol. 67, 2020, pp. 511–538, 10.1007/s40295-019-00167-2.

[12] D. Canales, S. M. Perera, A. Kurttisi, and B. Baker-McEvilly, "A Low-Complexity Algorithm to Determine Trajectories Within the Circular Restricted Three-Body Problem," *Journal of the Astronautical Sciences*, Vol. 70, No. 46, 2023, https://doi.org/10.1007/s40295-023-00416-5.

[13] B. Baker-McEvilly, H. Aluvihare, S. M. Perera, and D. Canales, "A Reduced-Complexity Trajectory Generation Algorithm for Three-Body Regimes with Minimum Predefined Data," *IEEE Transactions on Aerospace and Electronic Systems*, 2024, pp. 1–15, 10.1109/TAES.2024.3465502.

[14] E. Karepova and V. Petrakova, "The comparison of several approaches to the interpolation of a trajectory of a navigation satellite," *IOP Conference Series: Materials Science and Engineering*, Vol. 537, 06 2019, 10.1088/1757-899X/537/2/022054.

[15] M. Horemuz and J. Andersson, "Polynomial interpolation of GPS satellite coordinates," *GPS Solutions*, Vol. 10, 2006, pp. 67–72, https://doi.org/10.1007/s10291-005-0018-0.

[16] G. Nykiel, M. Figurski, and Z. Baldysz, "Comparison of GPS Precise Ephemerides Interpolation Methods," *15th International Multidisciplinary Scientific GeoConference*, 06 2015, 10.5593/SGEM2015/B22/S9.020.

[17] X. Xiao-li and X. Yong-qing, "Study on the Orbit Prediction Errors of Space Objects Based on Historical TLE Data," *Chinese Astronomy and Astrophysics*, Vol. 43, No. 4, 2019, pp. 563–578, https://doi.org/10.1016/j.chinastron.2019.11.007.

[18] L. Ma and M. Wang, "Influence of Ephemeris Error on GPS Single Point Positioning Accuracy," *Artificial Satellites*, Vol. 48, 2013, pp. 125–139, 10.2478/arsa-2013-0011.

[19] S. Scheuerle, *Low-Energy Transfers in the Bicircular Restricted Four-Body Problem*. PhD thesis, Purdue University, 2024.

[20] B. McCann, A. Anderson, M. Nazari, and D. Canales Garcia, "Circular restricted full three-body problem with rigid-body spacecraft dynamics in binary asteroid systems," *Celestial Mechanics and Dynamical Astronomy*, Vol. 136, 02 2024, 10.1007/s10569-024-10180-9.

[21] A. Anderson, B. McCann, D. Canales, and M. Nazari, "Orbit and Attitude Coupling in the Full Higher-Fidelity Ephemeris Model within the context of the Geometric Mechanics Framework," *33rd AAS/AIAA Space Flight Mechanics Meeting, Austin*, 2023.

[22] B. N. Datta, *Numerical Linear Algebra and Applications (Second Edition)*. SIAM, 2010.

[23] N. J. Higham, *Accuracy and Stability of Numerical Algorithms*. Philadelphia, USA: SIAM, 1996.